



OPEN

Enhanced sunlight driven photocatalytic activity of In_2S_3 nanosheets functionalized MoS_2 nanoflowers heterostructures

Jaspal Singh & R. K. Soni

Visible light-sensitive 2D-layered based photocatalytic systems have been proven one of the effective recent trends. We report the preparation of a 2D-layered based In_2S_3 - MoS_2 nanohybrid system through a facile hydrothermal method, capable of efficiently degrading of organic contaminants with remarkable efficiency. Transmission electron microscopy (TEM) results inferred the attachment of 2D-layered In_2S_3 sheets with the MoS_2 nanoflakes. Field emission SEM studies with chemical mapping confirm the uniform distribution of Mo, In, and S atoms in the heterostructure, affirming sample uniformity. X-ray diffraction, X-ray photoelectron spectroscopy, and Raman spectroscopy results confirm the appearance of 2H- MoS_2 and β - In_2S_3 in the grown heterostructures. UV-DRS results reveal a significant improvement in the optical absorbance and significant bandgap narrowing (0.43 eV) in In_2S_3 - MoS_2 nanohybrid compared to pristine In_2S_3 nanosheets in the visible region. The effective bandgap narrowing facilitates the charge transfer between MoS_2 and In_2S_3 and remarkably improves the synergistic effect. Effective bandgap engineering and improved optical absorption of In_2S_3 - MoS_2 nanohybrids are favorable for enhancing their charge separation and photocatalytic ability. The photocatalytic decomposition efficiency of the pristine In_2S_3 nanosheets and In_2S_3 - MoS_2 nanohybrids sample is determined by the decomposing of methylene blue and oxytetracycline molecules under natural sunlight. The optimized In_2S_3 - MoS_2 nanohybrids can decompose 97.67% of MB and 76.3% of OTC-HCl molecules solution in 8 min and 40 min of exposure of sunlight respectively. 2D-layered In_2S_3 - MoS_2 nanohybrids reveal the tremendous remediation performance towards chemical contaminations and pharmaceutical waste, which indicates their applicability in industrial and practical applications.

Visible light-sensitive photocatalyst has been extensively studied due to their tremendous performance for energy production and environmental remediation applications¹⁻⁵. Visible light-sensitive photocatalyst indicated the capability and usage of engineered nanostructures into the light-harvesting capability from natural sunlight. For more advanced and practical applications, photocatalyst material should be highly sensitive towards visible light, which can strongly absorb the visible spectrum from sunlight. Semiconductor-based photocatalysts have been proven to be one of the best ways to decomposed organic waste using light exposure after the outstanding discovery of water splitting by Fujishima in 1972⁶⁻¹⁵. The efficiency of semiconductor-based photocatalyst, however, is limited by insufficient light utilization and poor effective surface area. To overcome these issues, two-dimensional (2D) layered structured transition metal chalcogenides (TMDC) based photocatalysts have been developed, which tremendously absorb the visible light and also provide sufficient effective surface area¹⁶⁻¹⁸. In addition, layered structured TMDC based photocatalyst exhibits outstanding chemical, optical and electronic properties which make them unique for environmental remediation and energy production applications^{19,20}. Among various layered structures Indium sulfide (In_2S_3) has received significant attention recently in the field of visible light photocatalyst because of its low toxicity, high photo-stability, and narrow bandgap (2.0–2.3 eV)^{21,22}. On the other hand, the photocatalytic nature of In_2S_3 is found to be low due to the high recombination rate and poor mass transfer²³. Several parameters such as modulation in morphology, a surface area strongly influenced the photocatalytic activity of the In_2S_3 nanostructures by efficient charge separation, the improved lifetime of charge carriers, and high rate of mass transfer^{23,24}. Apart from this, various efforts, such as phase optimization^{25,26}, heterostructures creation^{27,28}, and noble metal nanoparticle functionalization^{29,30}, have been devoted to improving

Laser Spectroscopy Lab, Department of Physics, Indian Institute of Technology Delhi, Hauz Khas, New Delhi 110016, India. email: jaspal2125@gmail.com

the photodegradation capability of In_2S_3 nanostructures. 2D-TMDCs based heterostructures-based photocatalyst is one of the advanced and effective strategies to control the recombination rate and improve the photodegradation ability through synergistic effect between two layered nanostructures³¹. Nanostructured MoS_2 (band-gap ~ 1.9 eV) is extensively explored and employed for several applications such as sensing³², energy production³³, optoelectronic devices³⁴, and antibacterial activity³⁵. Due to its fascinating optical, electronic, and chemical properties. MoS_2 modified In_2S_3 based heterostructures can effectively enhance the lifetime of photoinduced charge carriers through synergistic effect among them³⁶. In_2S_3 nanosheets combined with MoS_2 nanoflowers is expected to increase the photoinduced catalytic activity^{37–39} due to sharing of the similar 2D layered structures by MoS_2 and In_2S_3 , which inferred the creation of high-quality, intimate heterojunction, and exhibits preferential band-gap alignments that help to generate the unsaturated radicals to enhance the rate of photocatalytic reactions. It has been found that the existence of MoS_2 can initiate the formation of superoxide radicals which is beneficial for the decomposition of organic molecules under light exposure^{40,41}. Moreover, MoS_2 presence in In_2S_3 can further enhance the active sites, which can effectively interact with the pollutant molecules. Li et al.²³ fabricated hierarchical $\text{In}_2\text{S}_3/\text{MoS}_2$ nanosheets using the exfoliation method with the hydrothermal method. The prepared $\text{In}_2\text{S}_3/\text{MoS}_2$ nanohybrids were embraced for photocatalytic application through the Aza-Henry reaction. They have demonstrated that $\text{In}_2\text{S}_3/\text{MoS}_2$ nanohybrids attained superior photocatalytic activity compared to pure MoS_2 and In_2S_3 . Sun et al.³¹ prepared $\text{MoS}_2/\text{In}_2\text{S}_3$ flakes-based photoanode by using a one-pot synthesis process and applied it for the H_2 production application. In their study, they have demonstrated the effective charge separation in $\text{MoS}_2/\text{In}_2\text{S}_3$ flakes for a high H_2 production rate.

2D-layered-based heterostructures are emerging as the new material for environmental remediation applications and are rarely reported in the literature. Removal of pharmaceutical and chemical waste has not been reported by using the 2D-layered In_2S_3 - MoS_2 nanohybrids-based photocatalyst. This study also highlights the contribution of improvement in the optical absorption and significant bandgap narrowing on the photodegradation nature of In_2S_3 - MoS_2 nanoheterostructures.

In this report, we highlight the synergistic effect due to the effective bandgap narrowing in 2D-layered-based heterostructures for pollutant removal. To employ the proposed strategy, 2D-layered-based In_2S_3 - MoS_2 nanoheterostructures were engineered using a hydrothermal method and determined their photodegradation capability to decompose the variety of organic pollutants molecules methylene blue and oxytetracycline under sunlight illumination. Chemical surface states, optical profile, and modulation in the morphologies are explored and assured in the hierarchical heterostructures of In_2S_3 and MoS_2 . In_2S_3 - MoS_2 nanoheterostructures exhibit a significantly superior photocatalytic nature as compared to pristine In_2S_3 nanostructures. We have tuned the heterojunction density by varying the amount of MoS_2 over In_2S_3 for a superior photodegradation process which provides the insight understanding to design the efficient photocatalyst. Apart from this, In_2S_3 - MoS_2 nanoheterostructures revealed significant reusability and stability, which indicate their possible applications for other sunlight-driven processes.

Experimental

Materials. Indium chloride, Hexaammonium heptamolybdate tetrahydrate, and thiourea were purchased from Sigma-Aldrich, while oxytetracycline (OTC HCl) and methylene blue (MB) were obtained from SRL, and Merck, respectively. All chemical reagents were employed as purchased.

Formation of β - In_2S_3 -2H- MoS_2 heterostructures photocatalyst. In the reaction process, initially, 20 mL of Hexaammonium heptamolybdate tetrahydrate (0.08 mM) was dropwise added into the 20 mL thiourea (0.18 mM) under constant stirring. Similarly, another solution contained 20 mL of indium chloride (0.24 mM) was dropwise added into the 20 mL thiourea solution. In the next step, both solutions were mixed in a conical flask under vigorous stirring, after confirming the formation of a uniform mixture, it was transferred to a Teflon container of 100 mL. The pH of the obtained solution was set at 6 by using 0.5 M NaOH solution. In the next step, the Teflon-lined stainless steel autoclave contained sample was held at 180 °C for 18 h. The obtained sample was treated with ethanol and DI water and collected by centrifugation process, and finally, placed at 80 °C in the oven. The pristine In_2S_3 and In_2S_3 - MoS_2 samples with tuneable MoS_2 density (0.16 mM and 0.24 mM) were generated by the above-mentioned process. For better understanding, pristine In_2S_3 and In_2S_3 - MoS_2 heterostructures (0.08 mM, 0.16 mM and 0.24 mM) hereafter reported as IP, IPM1, IPM2 and IPM3, respectively. The reaction process is depicted in Fig. 1.

Characterization techniques and photocatalysis reaction. Surface morphologies of pristine In_2S_3 and MoS_2 modified In_2S_3 samples were explored through scanning electron microscopy (ZEISS, EVO) combined with the elemental mapping facility, while transmission electron microscopy (JEOL-2100 F, Japan) was employed to determine the crystal structure of In_2S_3 - MoS_2 nanohybrids. Powder X-ray diffraction technique (Rigaku Ultima IV, Ri) was employed to investigate the diffraction patterns of In_2S_3 - MoS_2 nanohybrids. Optical studies of synthesized samples were explored by the UV-DRS (Shimadzu UV-2450) method, photoluminescence spectroscopy (RF-6000 Shimadzu), and Raman spectroscopy (Renishaw inVia). The chemical composition of In_2S_3 - MoS_2 nanohybrids was investigated through X-ray photoelectron spectroscopy (ESCA + Omicron Nano Technology). The photodegradation ability of MoS_2 functionalized In_2S_3 and pure In_2S_3 samples were explored by the breakdown of 10 μM MB solution and oxytetracycline (OTC-HCl) molecules in sunlight exposure (800 W/ m^2). Modulations in the intensity of the targeted pollutant molecules solutions with different photocatalyst samples for the same exposure time intervals (2, 4, 6, and 8 min) were measured using UV-Visible absorption spectroscopy (Perkin Elmer). In the photocatalytic reaction, the used amount of each photocatalyst sample is 2.5 mg/L. In order to explore the active species in the photodegradation reaction charge trapping studies were

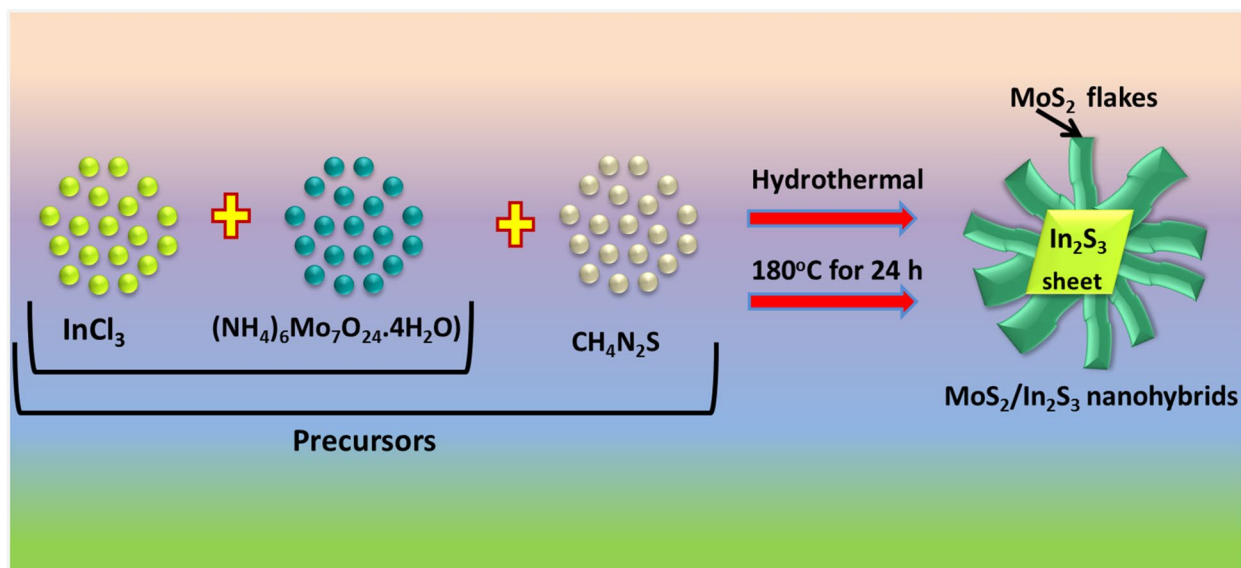


Figure 1. Depicts the fabrication process of In_2S_3 - MoS_2 nanohybrids.

performed. To trap the superoxide radicals, electrons, hydroxyl radicals, and holes four scavengers namely benzoquinone (BQ), copper nitrate (CN), formic acid (FA), and Isopropanol alcohol (IPA) were employed, respectively.

Results and discussion

Figure 2 illustrates the X-ray diffraction patterns of pristine In_2S_3 and MoS_2 modified In_2S_3 . XRD for sample IP indicates nine reflections (311), (222), (400), (422), (511), (440), (531), (553), and (622), which assured the presence of β -phase of In_2S_3 (JCPDS-500814). XRD spectrum for sample IPM1 shows eight diffraction patterns (311), (222), (400), (511), (440), (531), (533), and (622) corresponds to In_2S_3 while two peaks with reflection (100) and (106) assures the existence of 2H phase of MoS_2 (JCPDS-371492). XRD spectrum for sample IPM2 indicates similar diffraction peaks compared to the XRD curve of sample IPM1. Interestingly, the peak intensity of (100) and (106) peaks are found enhanced in sample IPM2 compared to sample IPM1 which inferred the high concentration of MoS_2 in In_2S_3 - MoS_2 nanohybrids. For sample IPM3, nine diffraction peaks (100), (311), (400), (511), (440), (531), (106), (553) and (622) can be appeared. Among them, seven peaks (311), (400), (511), (440), (531), (553), and (622) inferred the formation of In_2S_3 , while (100) and (106) indicate the presence of MoS_2 . XRD results assure the formation of In_2S_3 - MoS_2 nanohybrids in samples IPM1, IPM2 and, IPM3.

Raman spectra of sample IP, IPM1, IPM2, and IPM3 are presented in Fig. 3. Raman spectrum for sample IP indicating the four distinct peaks at 183 cm^{-1} , 249 cm^{-1} , 306 cm^{-1} and 369 cm^{-1} which are attributed to the fingerprint vibrations of β -phase of In_2S_3 ⁴². Raman result for sample IPM1 indicates the slight shift in the Raman peaks corresponds to the β -phase of In_2S_3 . The observed peaks are 195 cm^{-1} , 223 cm^{-1} , 305 cm^{-1} and 347 cm^{-1} implies the formation of MoS_2 - In_2S_3 nanohybrids^{23,38}. Apart from this, two distinct peaks at 379 cm^{-1} and 405 cm^{-1} arise in the Raman curve of sample IPM1, further confirmed the existence of MoS_2 . Raman spectrum for sample IPM2, the peaks correspond to the β - In_2S_3 and 2H- MoS_2 are found slightly shifted compared to Raman spectrum of sample IPM1. The observed peaks for sample IPM2 are 197 cm^{-1} , 221 cm^{-1} , 303 cm^{-1} , 343 cm^{-1} , 378 cm^{-1} and 403 cm^{-1} . Interestingly, it can be seen that the intensity of peaks at 378 cm^{-1} and 403 cm^{-1} is higher as than sample IPM1, which suggested the high-density MoS_2 in sample IPM2 as compared to sample IPM1. For sample IPM3, the Raman studies reveals the six peak at 197 cm^{-1} , 221 cm^{-1} , 304 cm^{-1} , 343 cm^{-1} , 378 cm^{-1} and 405 cm^{-1} . The intensity of two peaks for MoS_2 at 378 cm^{-1} and 405 cm^{-1} in sample IPM3 is higher than that of sample IPM1 and IPM2. The significant shift in the Raman peaks of sample IPM1, IPM2, and IPM3 compared to sample IP affirms the attachment of MoS_2 with In_2S_3 ³⁸. The shift in the Raman spectra of MoS_2 modified In_2S_3 can be ascribed due to the lattice vibrations enable through the variation in the bond force constant of Mo-S and In-S bond. Modulation in bond force constant generated due to the modification of Mo^{4+} atom in In_2S_3 ^{23,38,43}.

Figure 4a–d depicts the modulations in the morphologies of sample IP, IPM1, IPM2, and IPM3. For sample IP, 2D-nanosheets can appear with an average width of 162 nm (Fig. 4a). FESEM result for sample IPM1 illustrates the functionalization of 2D-layered structured aggregates on sheet-like nanostructures Fig. 4b. With the increment in the concentration of MoS_2 , a more distinct flower-like morphology can be seen in the FESEM image of sample IPM2. Apart from this, a 2D-layered sheet can also be seen attached to the surface of flowers-like morphology (Fig. 4c). To further increase the Mo^{4+} ions concentration in In_2S_3 , the 2D sheet mediated flowers-like structures attached with the sheet-like nanostructures can be observed for sample IPM3 (Fig. 4d). To confirm the formation of MoS_2 - In_2S_3 nanohybrids, elemental mapping for sample IPM3 was carried out and illustrated in Fig. 4e–i. The broader view of surface morphologies of sample IPM3 has been presented in Fig. 4e, while elemental mapping of the specific atom and corresponding nanohybrid is depicted in Fig. 4f–i. Elemental mapping

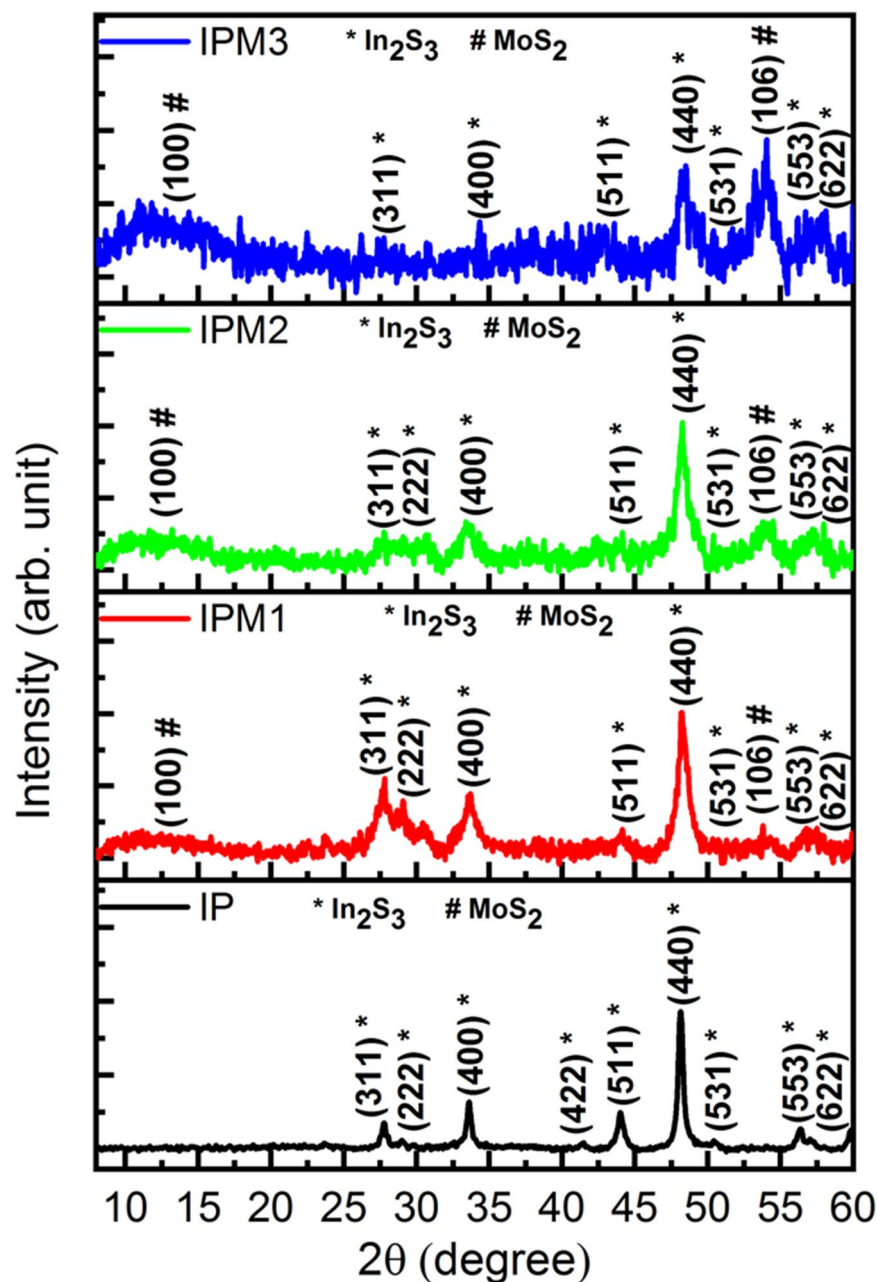


Figure 2. X-ray diffraction reflections of In_2S_3 nanosheets and In_2S_3 - MoS_2 nano hybrids.

studies affirm the uniform spreading of Mo, In, and S atoms in sample IPM3. Surface morphology results confirm the formation of MoS_2 - In_2S_3 nano hybrids. The EDX spectrum for sample IPM3 is presented in ((Fig. 1) supporting information). To explore the crystal structures and the attachment of In_2S_3 and MoS_2 , TEM and HRTEM studies were employed. Figure 5a–d shows the TEM images for sample IPM3 which inferred the presence of MoS_2 nanoflakes were attached with the In_2S_3 nanosheets. Figure 5c,d reveals the heterojunction creation among the MoS_2 nanoflakes and In_2S_3 sheets. TEM studies affirm that the assembly of MoS_2 nanosheets formed the flowers-like nanostructures on the surface of In_2S_3 sheets. To further assured the formation of In_2S_3 - MoS_2 nano-heterojunction, high-resolution TEM studies were performed and depicted in Fig. 5e,f. The evaluated distance among the inter-planer lattice fringes is 0.61 nm and 0.32 nm which implies the existence of MoS_2 (002) and In_2S_3 (311) in sample IPM3. Thus HRTEM results assured the creation of In_2S_3 - MoS_2 . The information regarding the structural profile of the pristine MoS_2 sample is represented in Fig. 2 supporting information).

The optical profile of pristine In_2S_3 nanosheets and MoS_2 modified In_2S_3 is illustrated in Fig. 6a. The optical absorption curve of sample IP reveals a broad peak form 250–600 nm. With the modification of MoS_2 in In_2S_3 , the optical absorption enhanced significantly (sample IPM1). For sample IPM2, the optical absorption is further increased and found higher than IP and IPM1. The optical absorption spectrum for sample IPM3 indicates the highest absorption compared to sample IP, IPM1, and IPM2. Optical absorption studies manifest a remarkable

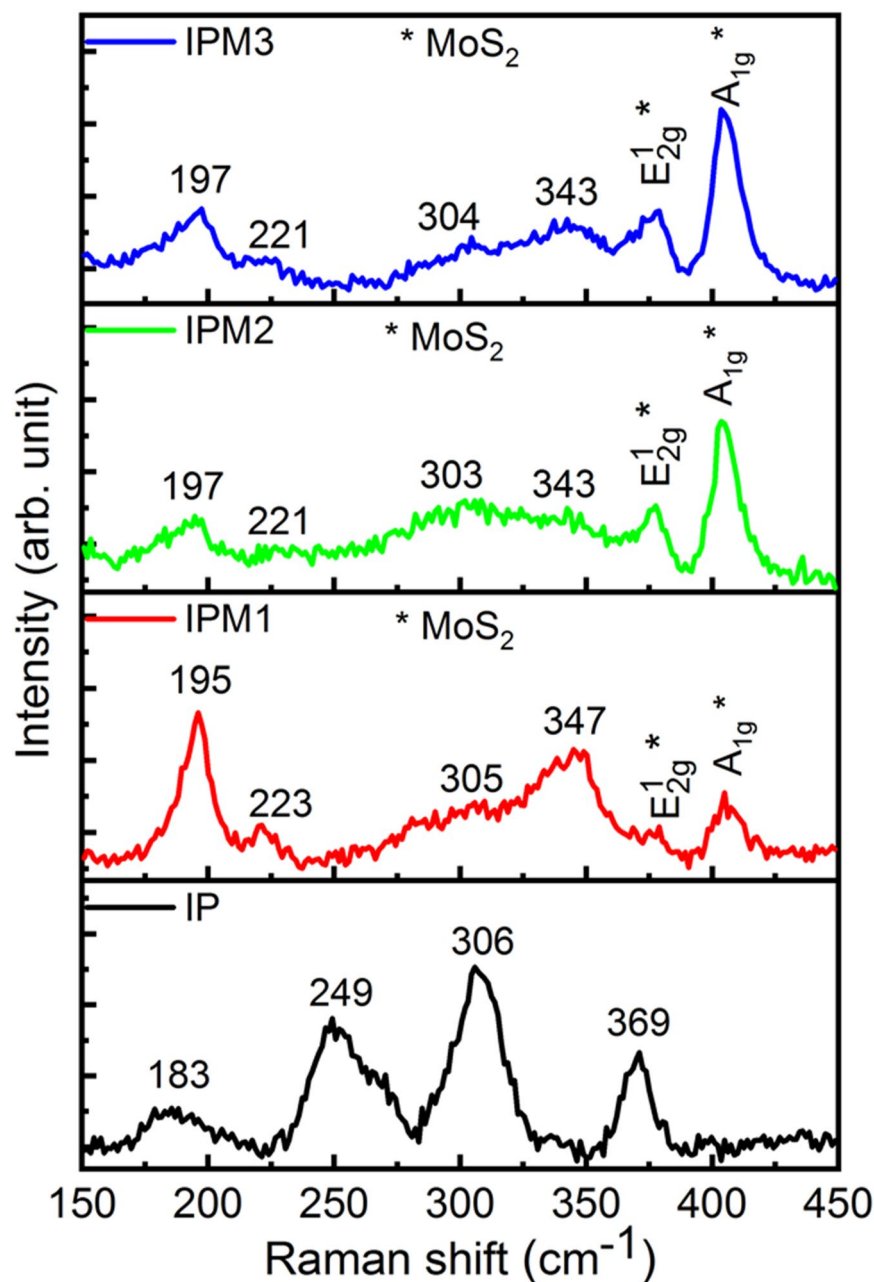


Figure 3. Raman results of In_2S_3 nanosheets and $\text{In}_2\text{S}_3\text{-MoS}_2$ nanohybrids.

improvement in $\text{MoS}_2\text{-In}_2\text{S}_3$ nanohybrids as compared to pristine In_2S_3 . To explore the bandgap engineering in $\text{MoS}_2\text{-In}_2\text{S}_3$ nanohybrids Tauc plots, studies were carried out and presented in Fig. 6b. Tauc plots suggest the narrowing in the bandgap in $\text{MoS}_2\text{-In}_2\text{S}_3$ nanohybrids as compared to pristine In_2S_3 . The computed bandgap for sample IP, IPM1, IPM2 and IPM3 are 2.25 eV, 1.94 eV, 1.89 eV and 1.82 eV, respectively.

The valance state and surface chemical composition of $\text{MoS}_2\text{-In}_2\text{S}_3$ nanohybrids were determined through the XPS and illustrated in Fig. 7. Gaussian fitted XPS spectra for In3d, S2p and Mo3d were presented in Fig. 7a–c, respectively. Figure 7a reveals that the XPS spectrum for In3d consists of two distinct peaks at 444.6 eV and 452.2 eV, which can be assigned to the $\text{In}3d_{5/2}$ and $\text{In}3d_{3/2}$, respectively⁴⁴. Gaussian fitted S2s spectrum reveals the three peaks at 161.8 eV, 164.3 eV and 168.2 eV (Fig. 7b). The peaks at 161.8 eV and 164.3 eV can be attributed to the $\text{S}2p_{3/2}$ and $\text{S}2p_{1/2}$ sequentially and affirms the presence of the S2p state of the sulfur atom^{38,39}. Apart from this, a broad peak at 168.2 eV assured the existence of the S–O bond⁴⁵. This bond inferred the partial oxidation of sulfur in the hydrothermal process^{45–47}. The fitted spectrum of Mo3d shows the distinct four peaks at 228.3 eV, 231.0 eV, 232.1 eV, and 234.5 eV (Fig. 7c). The major peaks at 228.4 eV and 231.3 eV corresponds to the $\text{Mo}3d_{5/2}$ and $\text{Mo}3d_{3/2}$, respectively⁴¹. The peaks at 232.1 eV and 234.5 eV can be attributed to the existence of Mo^{+6} states in the Mo3d spectrum^{46,48}. Both peaks arise due to the incomplete reduction of Mo precursors in hydrothermal reaction⁴⁸. Zou et al.⁴⁸ reported the formation of MoS_2/RGO nanocomposites through the hydrothermal method.

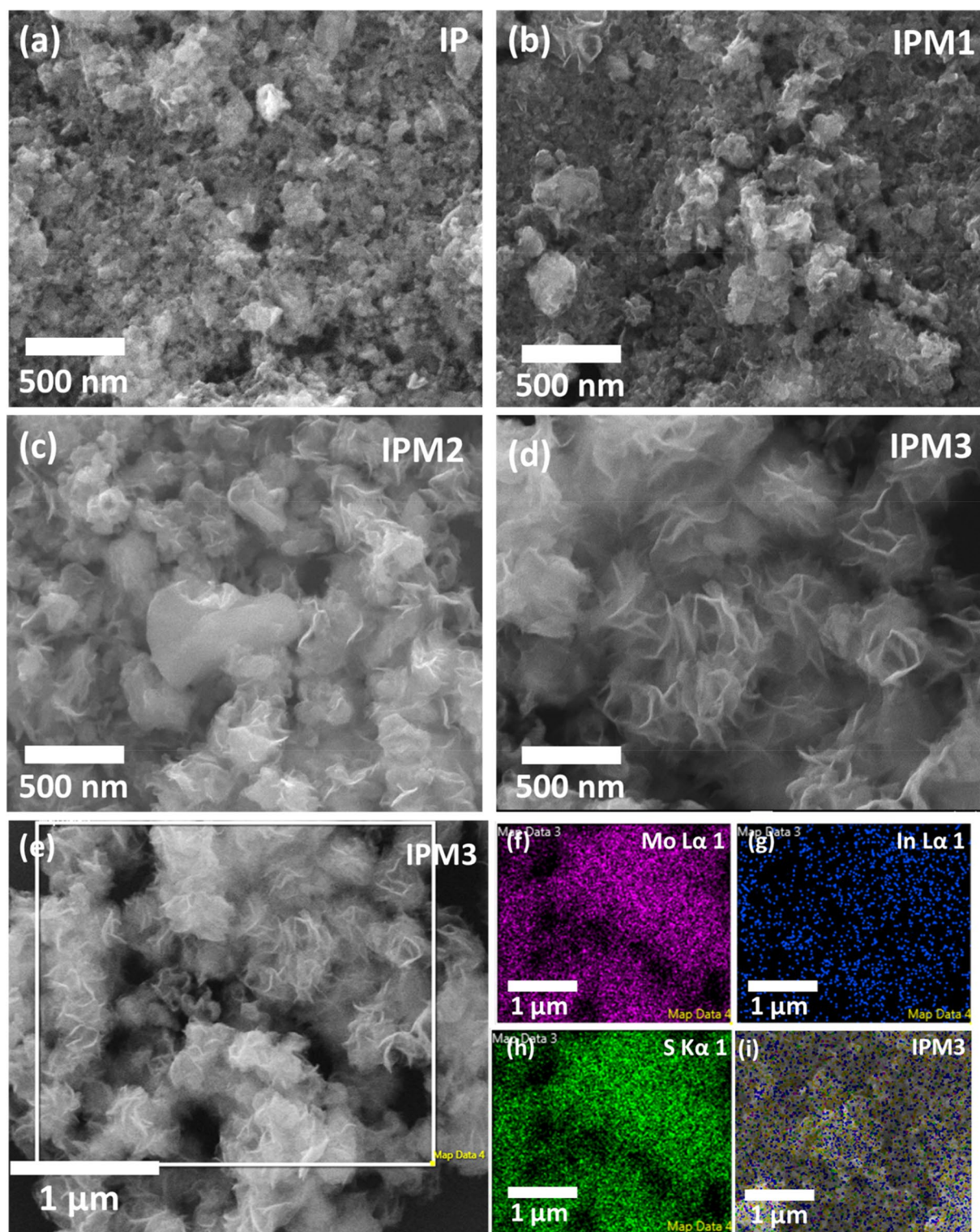


Figure 4. (a–d) FESEM images of sample IP, IPM1, IPM2, and IPM3 indicating the modulations in their morphology, (e) FESEM image of sample IPM3 revealing the formation of In_2S_3 nanosheet decorated MoS_2 nanoflowers, (f–h) Chemical mapping of sample IPM3 assuring the independent existence of In, Mo, and S atoms in sample IPM3, (i) Mapped image of sample IPM3 assuring the formation of $\text{In}_2\text{S}_3\text{-MoS}_2$.

In their XPS study, they have also observed the Mo^{+6} peaks due to incomplete reduction of Mo precursors. Moreover, it is possible that edges of the MoS_2 or defect state are bonded with oxygen and give rise to the peaks corresponds to the Mo^{+6} states⁴⁹. XPS studies indicate the presence of Mo, In, and S in the state of Mo^{+4} , In^{+3} ,

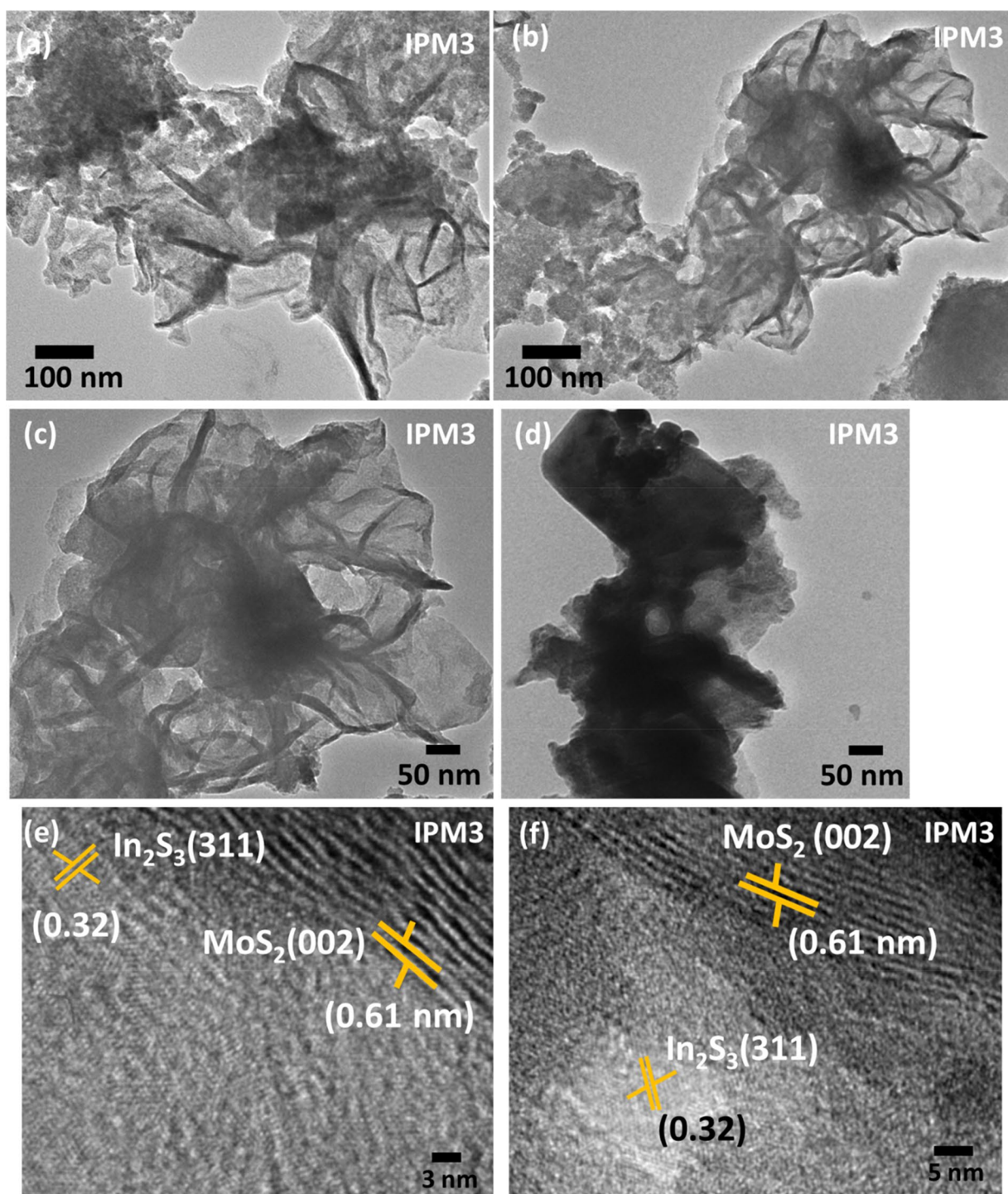


Figure 5. (a–d) TEM image of sample IPM3 revealing the formation of In_2S_3 nanosheet decorated MoS_2 nanoflowers, (e, f) High-resolution TEM images indicating fringes distance for MoS_2 and In_2S_3 .

and S^{2-} state in the MoS_2 – In_2S_3 nano hybrids, respectively. XPS results explicitly suggest that no shift takes place in the recombination process of MoS_2 – In_2S_3 nano hybrids.

We investigated the sunlight-induced photodegradation ability of the In_2S_3 nanosheets and MoS_2 modified In_2S_3 samples by the degradation of MB molecule solution. Figure 8a–d depicts the optical absorption spectrum of MB molecule solution employing sample IP, IPM1, IPM2, and IPM3. A UV–visible absorption study implies that sample IPM3 exhibits the highest photocatalytic efficiency compared to sample IP, IPM1, and IPM2. Sample IPM3 is found 96.8% efficient for the breakdown of $10\ \mu\text{M}$ MB molecule solution in 8 min, while sample IP, IPM1, and IPM2 are found capable of decomposing 35.3%, 77.7%, and 95.3% of $10\ \mu\text{M}$ MB molecule solution in 8 min (Fig. 9a). Figure 8e shows the modulations among the photodegradation kinetics of sample IP, IPM1, IPM2, and IPM3. The photodecomposition capability of pristine MoS_2 nanoflowers for MB pollutant molecules

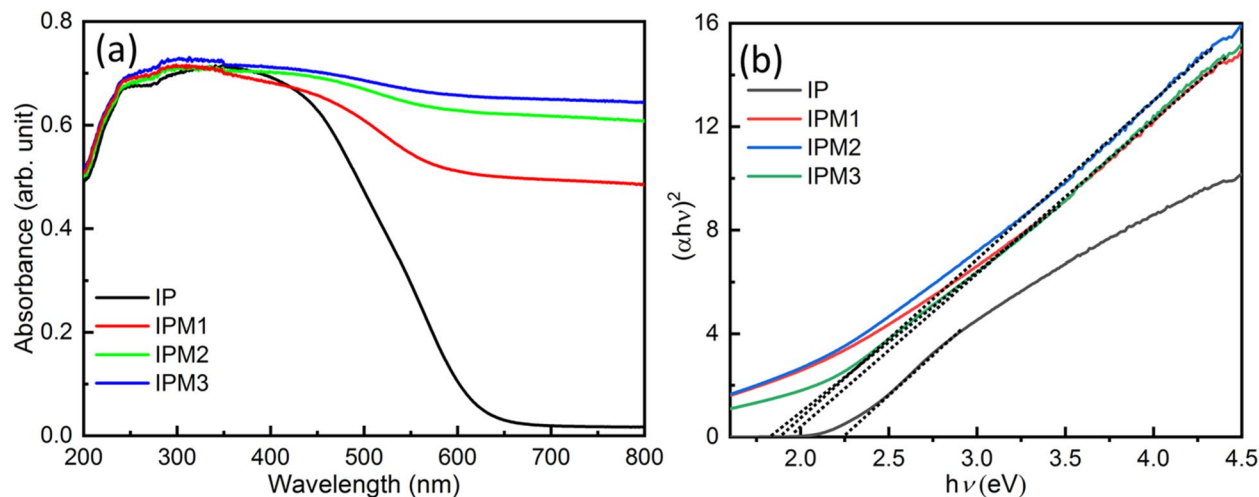


Figure 6. (a) UV-DRS studies depicting the variations in the optical absorbance profile for sample IP, IPM1, IPM2, and IPM3, (b) Tauc plots for sample IP, IPM1, IPM2, and IPM3.

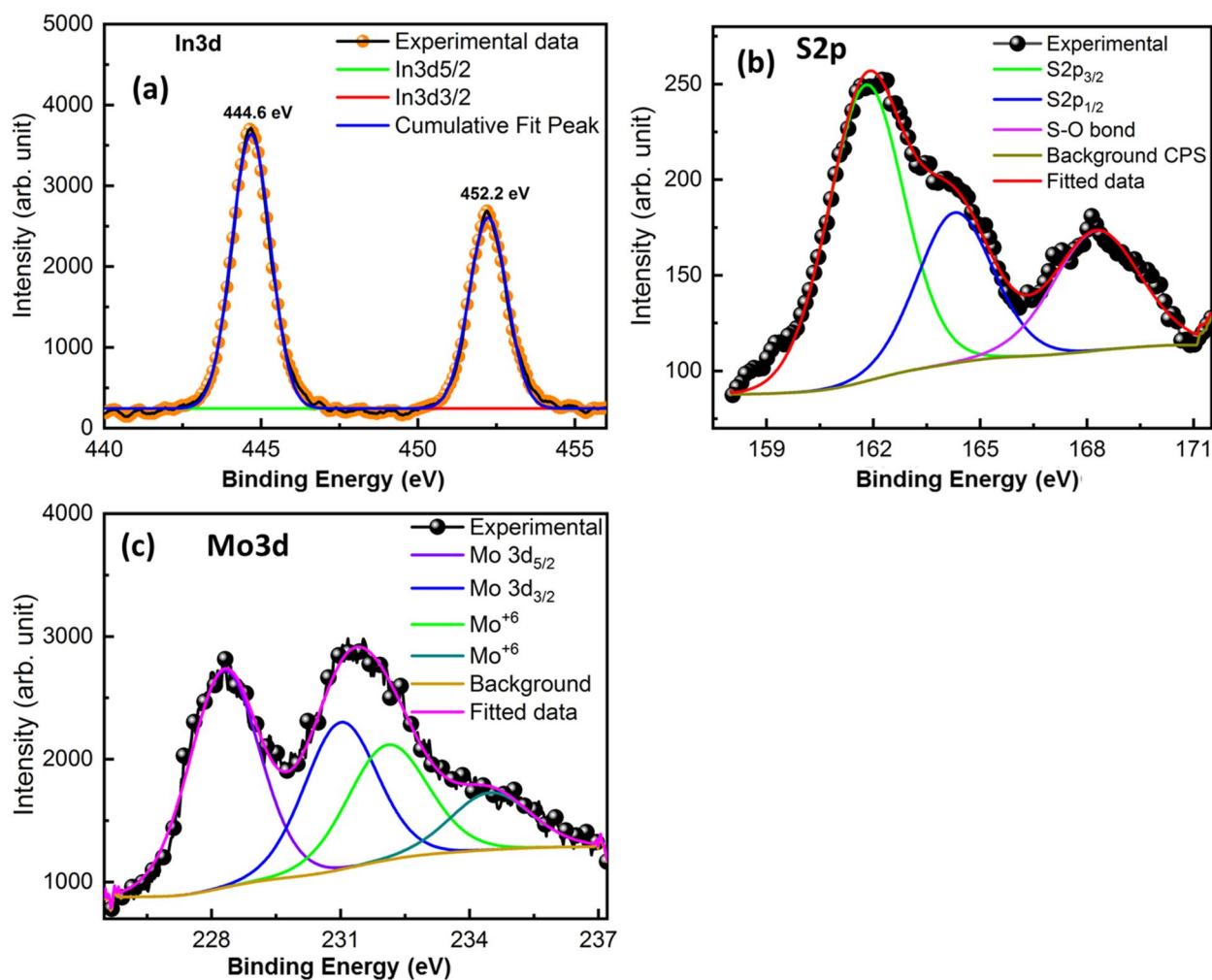


Figure 7. (a) Fitted XPS spectrum of In3d, (b) Fitted XPS spectrum of S2s, (c) Gaussian fitted XPS of Mo3d.

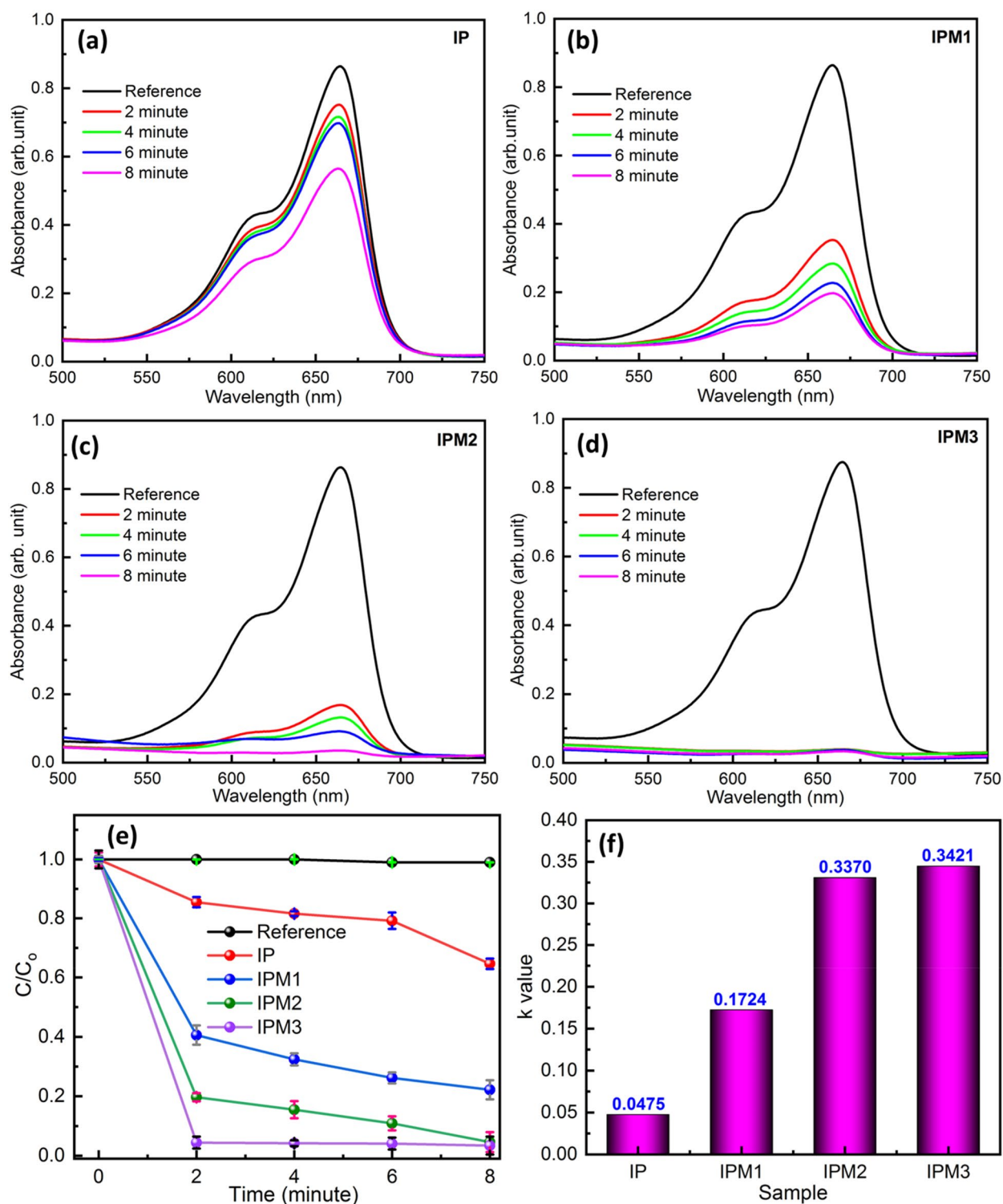


Figure 8. (a–d) Optical absorption spectra of MB molecule by employing different photocatalyst sample IP, IPM1, IPM2, and IPM3, (e) Photodegradation rate kinetics of MB molecule degradation by employing sample IP, IPM1, IPM2, and IPM3, (f) Rate constant (k) values of the breakdown of MB molecule solution using sample IP, IPM1, IPM2, and IPM3.

was measured and presented in (Fig. 3a supporting information). The calculated photodegradation efficiency of pristine MoS_2 is 62.2%. Photodegradation rate kinetics reveals the higher photodegradation performance of sample IPM3 as compared to other photocatalyst samples. In order to find out the rate constant value of each photocatalyst sample, linear fitting of logarithm value of C/C_0 as a function of exposure time were plotted. The

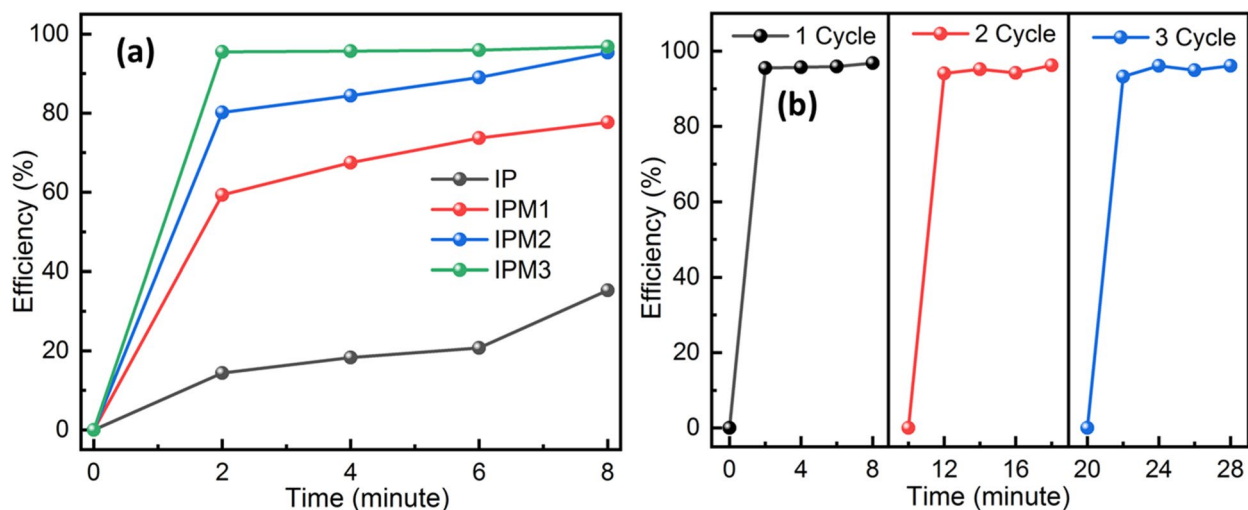


Figure 9. (a, b) Photodegradation efficiency of sample IP, IPM1, IPM2, and IPM3 under sunlight, (b) Reusable photocatalyst test for sample IPM3 indicating its stability.

rate constant value for sample IP, IPM1, IPM2, and IPM3 is depicted in Fig. 8f. The calculated k values for sample IP, IPM1, IPM2, and IPM3 are 0.0475/min, 0.1724/min, 0.357/min, and 0.3421/min, sequentially while the k value for pristine MoS_2 nanoflowers is found to be 0.1673/min (Fig. 3b supporting information). Photocatalytic studies affirm that sample IPM3 attain 2.70 times better photodecomposition performance as compared to pristine sample IP. The rate constant value for sample IPM3 is 7.2 times and 2.04 times the k value of sample IP and pristine MoS_2 . Photodecomposition results assure the improved degradation nature of the IPM3 sample as compared to other prepared photocatalyst samples. The stability of the most efficient synthesized sample (IPM3) was explored through the usage of sample IPM3 for three cycles of the photocatalytic reaction process. After three runs of photodegradation reaction, the efficiency of sample IPM3 is constant, which indicates their stable nature (Fig. 9b). To reveal the high photodegradation capability of the most efficient sample IPM3, the photodecomposition of OTC-HCl molecules was explored. Figure 10a,b indicates the optical absorption results of photodegradation results of OTC-HCl molecule solution using sample IP and IPM3, respectively. Photodegradation rate kinetics assures the high photodecomposition performance of sample IPM3 as compare to sample IP. It has been computed that sample IP can decompose the 27.1% efficient while sample IPM3 shows the decomposition of 76.3% of 0.3 mg/mL of OTC-HCl solution in sunlight (Fig. 10c). The k -values for sample IP and IPM3 are 0.00621/min and 0.0308/min sequentially (Fig. 10d).

To determine the charge transfer profile in In_2S_3 - MoS_2 nanohybrids during the photocatalytic reaction, a schematic diagram has been presented (Fig. 11). Under sunlight irradiation, In_2S_3 sheets and MoS_2 flakes are activated and generate the electron-hole pair in their respective conduction and valence bands. In the next step, the photoinduced electron in the conduction band of In_2S_3 moves towards the conduction band of MoS_2 due to the band alignment positions, which in turn maintain the synergistic effect and control the recombination rate in In_2S_3 nanosheets. The VB and CB positions for In_2S_3 nanosheets and MoS_2 nanoflakes are obtained through the following relation (1).

$$E_{CB} = \chi - E^e - 0.5E_g \quad (1)$$

where E_g indicates the bandgap value of the 2D layered materials (In_2S_3 and MoS_2) while E^e stands for the energy on the hydrogen scale (4.5 eV), and χ shows the electronegativity of the 2D layered nanostructures ($\text{In}_2\text{S}_3 \sim 4.7$ eV and $\text{MoS}_2 \sim 5.32$ eV). The computed VB and CB values for In_2S_3 nanosheets are 1.32 eV and -0.92 eV, sequentially, while CB and VB values for MoS_2 nanoflakes are -0.13 eV and 1.77 eV, sequentially.

Apart from the efficient charge separation process, the density of electrons in CB of MoS_2 enhanced remarkably; consequently, the formation rate of superoxide radicals increased. The high concentration of superoxide radicals primarily affects the photocatalytic reaction and accelerates it significantly. Similarly, due to the synergistic effect among In_2S_3 and MoS_2 , the enhanced production of holes interacted with the water molecule and created the hydroxyl radicals with high concentrations. The high density of hydroxyl radicals interacts with the MB molecule and degrades it. Thus the synergistic effect in In_2S_3 sheets- MoS_2 flakes control the charge separation and improve the photodegradation ability. To recognize the active species responsible for the improved photocatalytic activity of In_2S_3 - MoS_2 nanohybrids, charge trapping studies were embraced and presented in Fig. 4 (supporting information) Scavenger studies inferred that BQ and CN largely quench the rate of photocatalytic reaction kinetics of sample IPM3. Thus it can be concluded that superoxide and electrons majorly influence the photocatalytic reaction kinetics. In order to further determine the stability of sample IPM3 during the reusable photodegradation process, their structural characterization was explored and depicted in Fig. 5 (supporting information). Raman studies and TEM images assure the high stability of sample IPM3.

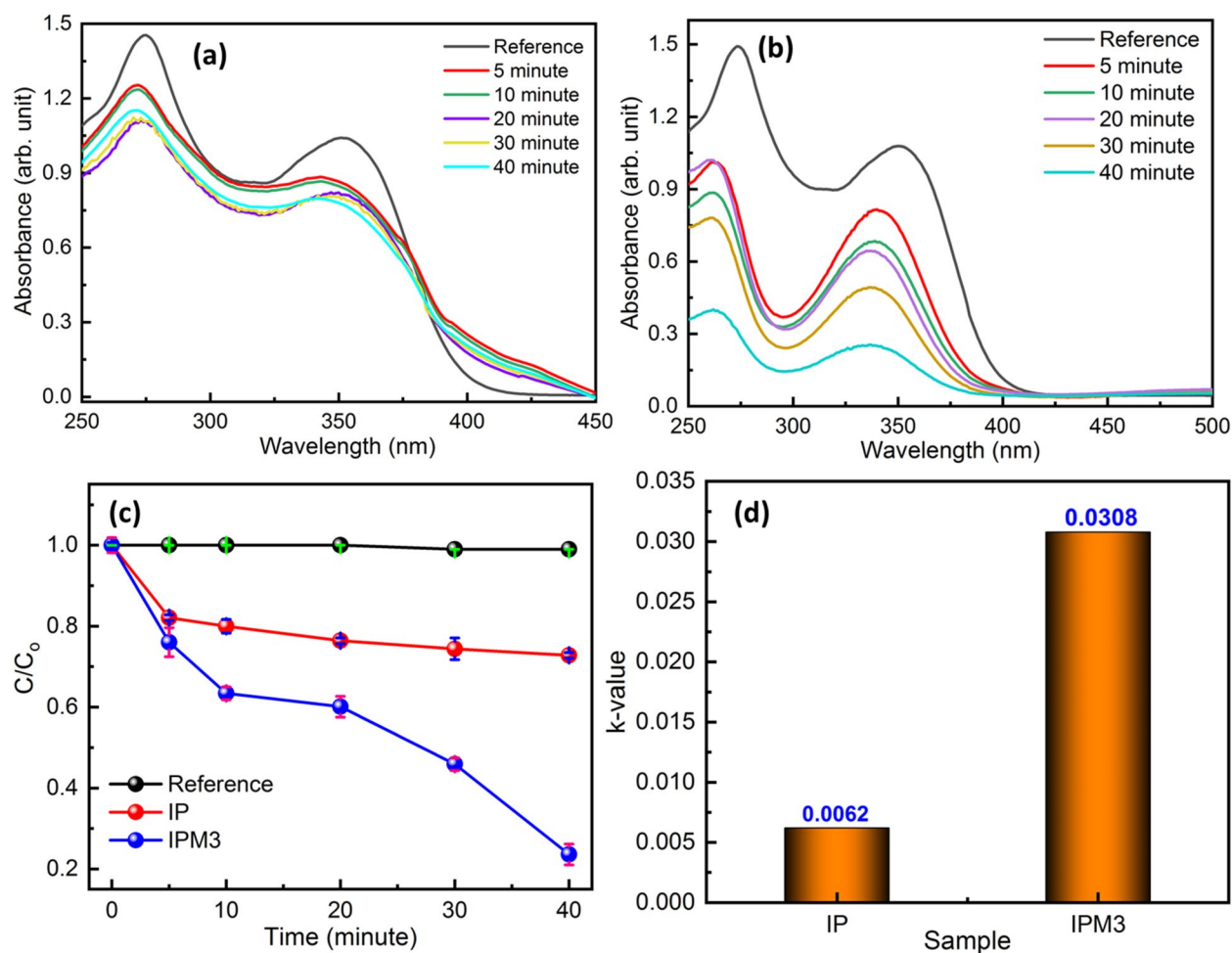


Figure 10. (a, b) Optical absorption spectra of OTC-HCl molecule by embracing IP and IPM3 photocatalyst respectively. (c) Degradation rate kinetics of OTC-HCl molecule using sample IP and IPM3, (d) Bar graph revealing the rate constant value for the breakdown of OTC-HCl molecule under sunlight using photocatalyst IP and IPM3.

In the present report, an In₂S₃-MoS₂ nano hybrids with an effective charge separation effect is successfully fabricated. The density of MoS₂ nanostructures over In₂S₃ nanosheets was precisely varied and used for the decomposition of MB and OTC molecules under solar light illumination.

The highest bandgap narrowing occurs in sample IPM3, which also indicates the efficient charge separation. Raman and XRD studies also reveal that the density of MoS₂ over In₂S₃ nanosheets was increased from sample IPM1 to IPM3. For sample IPM3, high numbers of heterojunction of MoS₂ and In₂S₃ are responsible for the extremely high sunlight-induced photodegradation capability towards MB molecules solution. Thus sample IPM3 decomposes 96.8% 10 μM of MB and 76.3% of 0.3 gm/mL OTC molecules solution in 8 min and 40 min sequentially under solar light illumination. Liu et al.³³ reported the formation of MoS₂ nanodots functionalized In₂S₃ nanoplates and used them for the photoelectrochemical application. They have found that MoS₂/In₂S₃ heterojunction with effective charge exhibited better performance as compared to pristine MoS₂ and In₂S₃. Wang et al.³⁴ synthesized MoS₂ functionalized In₂S₃ nanostructures for the Cr⁺⁶ removal using a photocatalysis process. They have demonstrated that MoS₂ functionalized In₂S₃ nanostructures exhibit 3.2 times better photocatalytic activity than pristine In₂S₃.

Conclusions

We have successfully engineered In₂S₃-MoS₂ nano hybrids using a simple hydrothermal method. The density of MoS₂ flakes was tuned over the surface of In₂S₃ nanosheets. Improvement in the optical absorption and significant bandgap narrowing tremendously contribute to improving the charge separation in 2D-layered In₂S₃-MoS₂ nano hybrids. Optimized In₂S₃-MoS₂ nano hybrids reveal the outstanding sunlight-driven photodecomposition performance for MB and OTC pollutant molecules solution. In₂S₃ nanosheets combined with the MoS₂ nano flakes decompose the 96.8% 10 μM of MB and OTC (0.3 mg/mL) solution in 8 min and 40 min, respectively. The photodecomposition capability of 2D-layered In₂S₃-MoS₂ nano hybrids was found 2.7 times higher as compared to pristine In₂S₃ nanosheets. Charge trapping studies inferred that superoxide radicals and electrons density majorly take part to improve the photodegradation ability of In₂S₃-MoS₂ nano hybrids. These results are very

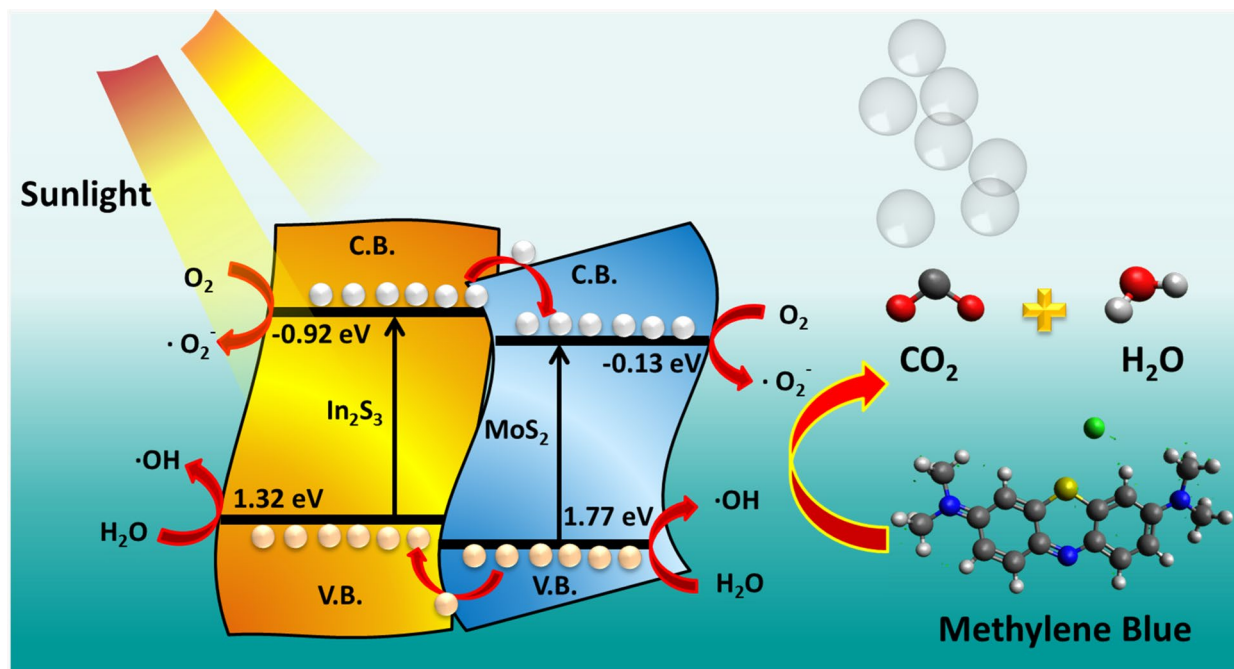


Figure 11. Energy level schematic diagram of In_2S_3 - MoS_2 nano hybrids depicting the synergistic effect among In_2S_3 nanosheets and MoS_2 nanoflowers under sunlight.

significant and unique, which demonstrated the outstanding photocatalytic activity of 2D layered In_2S_3 - MoS_2 nano hybrids towards chemical and pharmaceutical waste.

Received: 20 May 2021; Accepted: 19 July 2021

Published online: 28 July 2021

References

- Singh, J., Kumar, S. & Soni, R. K. Synthesis of 3D- MoS_2 nanoflowers with tunable surface area for the application in photocatalysis and SERS based sensing. *J. Alloys Compd.* **849**, 156502 (2020).
- Singh, J., Kumar, S., Verma, H. K. & Soni, R. K. Cost-effective scalable synthesis of few layers MoS_2 based thin film for sunlight enforced photocatalytic activity. *Opt. Mater.* **110**, 110506 (2020).
- Singh, J., Juneja, S., Soni, R. K. & Bhattacharya, J. Sunlight mediated enhanced photocatalytic activity of TiO_2 nanoparticles functionalized CuO - Cu_2O nanorods for removal of methylene blue and oxytetracycline hydrochloride. *J. Coll. Interface Sci.* **590**, 60–71 (2021).
- Singh, J. & Soni, R. K. Two-dimensional MoS_2 nanosheet-modified oxygen defect-rich TiO_2 nanoparticles for light emission and photocatalytic applications. *New J. Chem.* **44**, 14936–14946 (2020).
- Rengaraj, S. *et al.* Self-assembled mesoporous hierarchical-like In_2S_3 hollow microspheres composed of nanofibers and nanosheets and their photocatalytic activity. *Langmuir* **27**, 5534–5541 (2011).
- Fujishima, A. & Honda, K. Electrochemical photolysis of water at a semiconductor electrode. *Nature* **238**, 37–38 (1972).
- Lin, G. & Xu, X. Ba-Modified LaTiO_2N as an efficient visible light active photocatalyst for water oxidation. *ACS Sustain. Chem. Eng.* **8**, 9641–9649 (2020).
- Xu, X., Wang, R., Sun, X., Lv, M. & Ni, S. Layered perovskite compound NaLaTiO_4 modified by nitrogen doping as a visible light active photocatalyst for water splitting. *ACS Catal.* **10**, 9889–9898 (2020).
- Shen, Q. *et al.* Hollow dodecahedral structure of In_2O_3 - In_2S_3 heterojunction encapsulated by N-Doped C as an excellent visible-light-active photocatalyst for organic transformation. *Inorg. Chem.* **59**, 17650–17658 (2020).
- Zhang, J. *et al.* Defect engineering in atomic-layered graphitic carbon nitride for greatly extended visible-light photocatalytic hydrogen evolution. *ACS Appl. Mater. Interfaces* **12**, 13805–13812 (2020).
- Dong, S. *et al.* Fabrication of 3D ultra-light graphene aerogel/ Bi_2WO_6 composite with excellent photocatalytic performance: A promising photocatalysts for water purification. *J. Taiwan Inst. Chem. Eng.* **97**, 288–296 (2019).
- Dong, S. *et al.* Double-shelled ZnSnO_3 hollow cubes for efficient photocatalytic degradation of antibiotic wastewater. *Chem. Eng. J.* **384**, 123279 (2020).
- Dong, S. *et al.* A novel and high-performance double Z-scheme photocatalyst ZnO - SnO_2 - Zn_2SnO_4 for effective removal of the biological toxicity of antibiotics. *J. Hazard. Mater.* **399**, 123017 (2020).
- Dong, S. *et al.* Visible-light responsive PDI/rGO composite film for the photothermal catalytic degradation of antibiotic wastewater and interfacial water evaporation. *Appl. Catal. B Environ.* **291**, 120127 (2021).
- Dong, S. *et al.* Interfacial and electronic band structure optimization for the adsorption and visible-light photocatalytic activity of macroscopic ZnSnO_3 /graphene aerogel. *Compos. Part B Eng.* **215**, 108765 (2021).
- Xiang, Q., Cheng, F. & Lang, D. Hierarchical layered WS_2 /graphene-modified CdS nanorods for efficient photocatalytic hydrogen evolution. *Chemosuschem* **9**, 996–1002 (2016).
- Fu, S. *et al.* Few-layer WS_2 modified BiOBr nanosheets with enhanced broad-spectrum photocatalytic activity towards various pollutants removal. *Sci. Total Environ.* **694**, 133756 (2019).
- Fu, S. *et al.* A novel 0D/2D WS_2 / BiOBr heterostructure with rich oxygen vacancies for enhanced broad-spectrum photocatalytic performance. *J. Coll. Interface Sci.* **569**, 150–163 (2020).

19. Wang, Y. H., Huang, K. J. & Wu, X. Recent advances in transition-metal dichalcogenides based electrochemical biosensors: A review. *Biosens. Bioelectron.* **97**, 305–316 (2017).
20. Liu, Y., Duan, X., Huang, Y. & Duan, X. Two-dimensional transistors beyond graphene and TMDCs. *Chem. Soc. Rev.* **47**, 6388–6409 (2018).
21. Batabyal, S. K., Lu, S. E. & Vittal, J. J. Synthesis, characterization, and photocatalytic properties of In_2S_3 , ZnIn_2S_4 , and CdIn_2S_4 nanocrystals. *Cryst. Growth Des.* **16**, 2231–2238 (2016).
22. Mughal, M. A., Engelken, R. & Sharma, R. Progress in indium(III) sulfide(In_2S_3) buffer layer deposition techniques for CIS, CIGS, and CdTe-based thin film solar cells. *Sol. Energy* **120**, 131–146 (2015).
23. Li, Z. *et al.* Hierarchical photocatalyst of In_2S_3 on exfoliated MoS_2 nanosheets for enhanced visible-light-driven Aza-Henry reaction. *Appl. Catal. B: Environ.* **237**, 288–294 (2018).
24. Yang, S. *et al.* Ca(II) doped $\beta\text{-In}_2\text{S}_3$ hierarchical structures for photocatalytic hydrogen generation and organic dye degradation under visible light irradiation. *J. Coll. Interface Sci.* **491**, 230–237 (2017).
25. Sharma, R. K. *et al.* Adsorption-driven catalytic and photocatalytic activity of phase tuned In_2S_3 nanocrystals synthesized via ionic liquids. *ACS Appl. Mater. Interfaces* **9**, 11651–11661 (2017).
26. Nayak, A. K., Lee, S., Sohn, Y. & Pradhan, D. Synthesis of In_2S_3 microspheres using a template-free and surfactant-less hydrothermal process and their visible light photocatalysis. *CrystEngComm* **16**, 8064–8072 (2014).
27. Baral, B., Mansingh, S., Reddy, K. H., Bariki, R. & Parida, K. Architecting a double charge-transfer dynamics $\text{In}_2\text{S}_3/\text{BiVO}_4$ n–n isotype heterojunction for superior photocatalytic oxytetracycline hydrochloride degradation and water oxidation reaction: Unveiling the association of physicochemical, electrochemical, and photocatalytic properties. *ACS Omega* **5**, 5270–5284 (2020).
28. Yang, M. Q., Weng, B. & Xu, Y. J. Improving the visible light photoactivity of In_2S_3 -graphene nanocomposite via a simple surface charge modification approach. *Langmuir* **29**, 10549–10558 (2013).
29. Yan, T. *et al.* Ultra-low loading of Ag_3PO_4 on hierarchical In_2S_3 microspheres to improve the photocatalytic performance: The cocatalytic effect of Ag and Ag_3PO_4 . *Appl. Catal. B: Environ.* **202**, 84–94 (2017).
30. Wang, F. *et al.* Probing the charge separation process on $\text{In}_2\text{S}_3/\text{Pt-TiO}_2$ nanocomposites for boosted visible-light photocatalytic hydrogen production. *Appl. Catal. B: Environ.* **198**, 25–31 (2016).
31. Sun, B., Shan, F., Jiang, X., Ji, X. & Wang, F. One-pot synthesis of $\text{MoS}_2/\text{In}_2\text{S}_3$ ultrathin nanoflakes with mesh-shaped structure on indium tin oxide as photocathode for enhanced photo- and electrochemical hydrogen evolution reaction. *Appl. Surf. Sci.* **435**, 822–831 (2018).
32. Zhang, W., Zhang, P., Su, Z. & Wei, G. Synthesis and sensor applications of MoS_2 -based nanocomposites. *Nanoscale* **7**, 18364–18378 (2015).
33. Theerthagiri, J. *et al.* Recent advances in MoS_2 nanostructured materials for energy and environmental applications—a review. *J. Solid State Chem.* **252**, 43–71 (2017).
34. Wang, H., Li, C., Fang, P., Zhang, Z. & Zhang, J. Z. Synthesis, properties, and optoelectronic applications of two-dimensional MoS_2 and MoS_2 -based heterostructures. *Chem. Soc. Rev.* **47**, 6101–6127 (2018).
35. Pandit, S., Karunakaran, S., Boda, S. K., Basu, B. & De, M. High antibacterial activity of functionalized chemically exfoliated MoS_2 . *ACS Appl. Mater. Interfaces* **8**, 31567–31573 (2016).
36. Fang, Z. *et al.* Dual-defective strategy directing in situ assembly for effective interfacial contacts in MoS_2 cocatalyst/ In_2S_3 light harvester layered photocatalysts. *J. Mater. Chem. A* **4**, 13980–13988 (2016).
37. Sheng, W., Song, Y., Dou, M., Ji, J. & Wang, F. Constructing 1D hierarchical heterostructures of $\text{MoS}_2/\text{In}_2\text{S}_3$ nanosheets on CdS nanorod arrays for enhanced photoelectrocatalytic H_2 evolution. *Appl. Surf. Sci.* **436**, 613–623 (2018).
38. Liu, F. *et al.* MoS_2 nanodot decorated In_2S_3 nanoplates: A novel heterojunction with enhanced photoelectrochemical performance. *Chem. Commun.* **52**, 1867–1870 (2016).
39. Wang, L. & Zan, L. Noble metal-free MoS_2 -modified In_2S_3 for excellent visible-NIR-light-driven photocatalytic of Cr^{6+} removal in alkaline wastewater. *J. Nanoparticle Res.* **22**, 1–12 (2020).
40. Li, Z. *et al.* Utilization of MoS_2 and graphene to enhance the photocatalytic activity of Cu_2O for oxidative CC bond formation. *Appl. Catal. B Environ.* **213**, 1–8 (2017).
41. Jiang, W. *et al.* Photocatalytic hydrogen generation on bifunctional ternary heterostructured $\text{In}_2\text{S}_3/\text{MoS}_2/\text{CdS}$ composites with high activity and stability under visible light irradiation. *J. Mater. Chem. A* **3**, 18406–18412 (2015).
42. Zhao, Y. *et al.* Thickness-dependent optical properties and in-plane anisotropic Raman response of the 2D $\beta\text{-In}_2\text{S}_3$. *Adv. Opt. Mater.* **7**, 1901085 (2019).
43. Feth, S., Gibbs, G. V., Boisen, M. B. & Myers, R. H. Promolecule radii for nitrides, oxides, and sulfides: A comparison with effective ionic and crystal radii. *J. Phys. Chem.* **97**, 11445–11450 (1993).
44. Gao, W. *et al.* In_2S_3 nanomaterial as a broadband spectrum photocatalyst to display significant activity. *Appl. Catal. B Environ.* **176**, 83–90 (2015).
45. Li, B. *et al.* Preparation of monolayer MoS_2 quantum dots using temporally shaped femtosecond laser ablation of bulk MoS_2 targets in water. *Sci. Rep.* **7**, 1–12 (2017).
46. Wang, H. W., Skeldon, P. & Thompson, G. E. XPS studies of MoS_2 formation from ammonium tetrathiomolybdate solutions. *Surf. Coat. Technol.* **91**, 200–207 (1997).
47. Liu, J., Li, Y., Ke, J., Wang, Z. & Xiao, H. Synergically improving light harvesting and charge transportation of TiO_2 nanobelts by deposition of MoS_2 for enhanced photocatalytic removal of Cr(VI). *Catalysts* **7**, 30 (2017).
48. He, G., Zhang, Y. & He, Q. MoS_2/CdS heterostructure for enhanced photoelectrochemical performance under visible light. *Catalysts* **9**, 19–21 (2019).
49. Qiao, X., Hu, F., Hou, D. & Li, D. PEG assisted hydrothermal synthesis of hierarchical MoS_2 microspheres with excellent adsorption behavior. *Mater. Lett.* **169**, 241–245 (2016).

Acknowledgements

Jaspal Singh gratefully acknowledges the financial support of IIT Delhi through the IPDF fellowship.

Author contributions

J.S.: Conceptualization, Investigation, Writing—original draft. R.K.S.: Supervision, Writing—review and editing.

Competing interests

The authors declare no competing interests.

Additional information

Supplementary Information The online version contains supplementary material available at <https://doi.org/10.1038/s41598-021-94966-z>.

Correspondence and requests for materials should be addressed to J.S.

Reprints and permissions information is available at www.nature.com/reprints.

Publisher's note Springer Nature remains neutral with regard to jurisdictional claims in published maps and institutional affiliations.



Open Access This article is licensed under a Creative Commons Attribution 4.0 International License, which permits use, sharing, adaptation, distribution and reproduction in any medium or format, as long as you give appropriate credit to the original author(s) and the source, provide a link to the Creative Commons licence, and indicate if changes were made. The images or other third party material in this article are included in the article's Creative Commons licence, unless indicated otherwise in a credit line to the material. If material is not included in the article's Creative Commons licence and your intended use is not permitted by statutory regulation or exceeds the permitted use, you will need to obtain permission directly from the copyright holder. To view a copy of this licence, visit <http://creativecommons.org/licenses/by/4.0/>.

© The Author(s) 2021